Quench-induced nonequilibrium dynamics of spinor gases in a moving lattice

Z. N. Hardesty-Shaw,[1] Q. Guan,[2,3,4] J. O. Austin,[1] D. Blume,[2,3] R. J. Lewis-Swan,[2,3,*] and Y. Liu[1,†]
[1]*Department of Physics, Oklahoma State University, Stillwater, Oklahoma 74078, USA*
[2]*Homer L. Dodge Department of Physics and Astronomy, The University of Oklahoma, Norman, Oklahoma 73019, USA*
[3]*Center for Quantum Research and Technology, The University of Oklahoma, Norman, Oklahoma 73019, USA*
[4]*Department of Physics and Astronomy, Washington State University, Pullman, Washington 99164, USA*

(Received 14 December 2022; revised 10 April 2023; accepted 21 April 2023; published 16 May 2023)

The isolation and control of disparate degrees of freedom underpins quantum simulators. We advance the programmability of cold atom quantum simulators with a realization of the dynamic coupling of spatial and spin degrees of freedom. We experimentally demonstrate that violent spatial evolutions tune long-lived coherent spin dynamics and develop a model of quantum spin mixing incorporating the spatial evolution via time-dependent spin-spin interactions. Our results may open new paths towards the simulation of quantum spin models with tunable interactions via tailored spatial dynamics.

DOI: 10.1103/PhysRevA.107.053311

I. INTRODUCTION

Ultracold quantum gases that feature spatial and spin degrees of freedom offer a powerful platform for simulating quantum magnetism in controlled, isolated settings [1–5]. When combined with optical lattices, these simulation capabilities are exemplified by experimental studies featuring tunable dimensionality and filling factors [6–9]. Possessing long coherence times, these systems also provide an ideal platform for studying out-of-equilibrium phenomena such as spin mixing [10–13], transport [14,15], dynamical phases of matter [16], and critical dynamics across quantum phase transitions [7,8,17]. Simultaneously, advances in spin- and spatially-resolved probes [7,9,18,19] and the control of time- and spin-dependent lattice potentials are opening up new opportunities, including the study of multistate tunneling physics [20] and driven-dissipative phases [21], in the presence of the spin degree of freedom.

Typically, the energy scales of the spin and spatial degrees of freedom are disparate. This has been exploited to obtain a reduced description of the spin dynamics governed by a spin-spin interaction coefficient c_2 that depends only on a spatial profile that remains frozen due to, e.g., a strong confining potential [11,16,22–28]. In the context of spinor Bose-Einstein condensates (BECs), this decoupled regime has received significant attention [29–31] and, amongst other applications, has been utilized to generate entangled states in the highly controllable spin degree of freedom [32–37], which can also be mapped to the motional degrees of freedom [38–40].

In contrast, the interplay of spatial and spin degrees of freedom remains largely unexplored and, although typically weak, can provide a powerful avenue for controlling the spin dynamics through tailored dynamical manipulation of the spatial properties of the gas [41–45]. We provide an example of how spatial degrees of freedom can be utilized to manipulate the spin dynamics. We experimentally observe that a one-dimensional (1D) moving lattice, combined with a skew optical dipole trap (ODT), induces violent transient spatial motion, which is nevertheless accompanied by long-lived spin-mixing dynamics. We develop a theoretical understanding of these observations based on a *dynamical single spatial-mode approximation* (dSMA), which leads to an effective spin model with a time-dependent spin-spin interaction coefficient that depends on the temporal evolution of the BEC density profile. Experimental observations—including a robust critical regime featuring divergent timescales for the spin dynamics, which is tuned by the applied moving optical lattice and associated spatial motion—are qualitatively described by our model.

Our results open the way for the exploitation of classical spatial dynamics for simulating many-body quantum spin dynamics with highly tunable, time-dependent interactions [46,47], thereby enhancing the class of quantum spin models accessible in spinor BECs. In addition, our findings imply that spatial dynamics can provide new control knobs for the nonequilibrium generation of entangled spin states for, e.g., quantum-enhanced sensing [38].

The remainder of this paper is organized as follows. Section II discusses the experimental setup, the observed spin dynamics, and a first interpretation within a static single spatial-mode approximation (sSMA). Section III introduces the dSMA, which provides a more rigorous description of the observed spin dynamics. Section IV presents a combined experiment-theory analysis of the spatial dynamics, which are critical to understanding the spin dynamics. Finally, we conclude in Sec. V.

II. EXPERIMENTAL SETUP AND SPIN DYNAMICS

Each experimental cycle begins with a sodium spin-1 BEC at quadratic Zeeman energy q in an ODT (see Appendix A). A key feature of spinor BECs is their spin degree of freedom,

---

[*] lewisswan@ou.edu
[†] yingmei.liu@okstate.edu

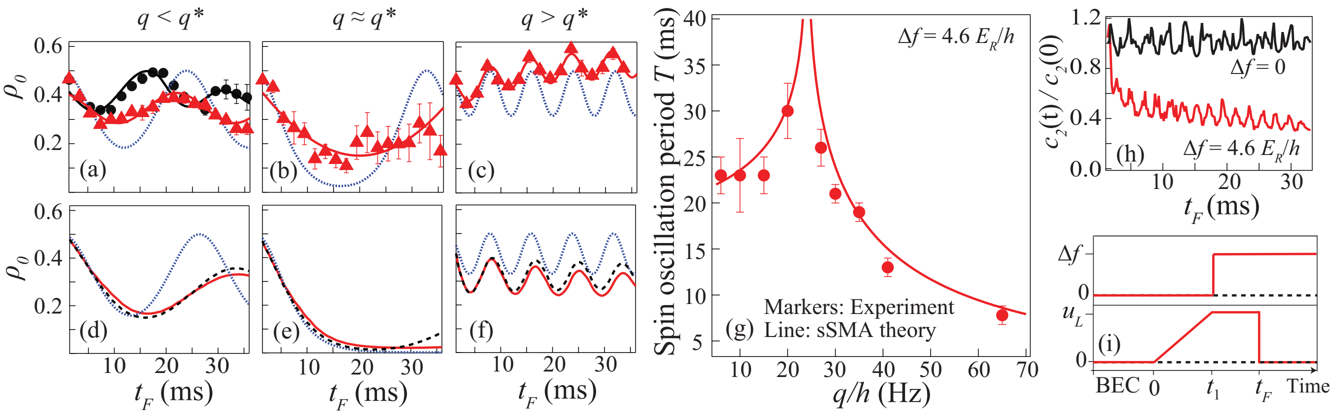

FIG. 1. (a)–(f) Exemplary time traces of ρ_0 for spinor BECs. Panels (a)–(c) show experimental results for ρ_0 (red markers) at $q/h = 15$ Hz (a), 25 Hz (b), and 65 Hz (c) as well as sSMA predictions (dotted lines) with $c_{2,\mathrm{fit}}/h = 23.7(1)$Hz extracted from Fig. 1(g). Panel (a) compares static (black) and moving (red) lattice results. Solid lines are sinusoidal fits to guide the eye. Panels (d)–(f) compare predicted ρ_0 for $q/h = 15$ Hz (d), 22 Hz (e), and 65 Hz (f) from 1D GP simulations (solid lines) to sSMA (dotted lines) with c_2 obtained through fits to the GP data (see Appendix D), and dSMA (dashed lines) with $c_2(t)$ obtained from GP data. The chosen q values exemplify the interaction dominated ($q < q^*$) and Zeeman ($q > q^*$) regimes separated by the critical region $q \approx q^*$. (g) Observed T (markers) vs q fit by analytical sSMA expressions (solid line) with the fitting parameter $c_{2,\mathrm{fit}}/h = 23.7(1)$Hz (see Appendix D). (h) Red (black) lines are evolution of $c_2(t)/c_2(0)$ for $q/h = 15$ Hz obtained from 1D GP simulations of the moving (static) lattice. All moving lattice data use a lattice depth $u_L = 2.3E_R$, $t_1 = 1.43$ms, and fixed $\Delta f = 4.6E_R/h$. (i) Timeline of the lattice depth (lower panel) and moving lattice speed (upper panel).

which is characterized by the spin-dependent interaction coefficient c_2. Spin mixing and other nonequilibrium phenomena driven by a static c_2 have been studied in various contexts [7,8,11,23,24,28,31]. Here, in contrast, we demonstrate that c_2 can be tuned dynamically by utilizing a moving lattice to change the BEC's spatial density profile. We construct a 1D moving lattice with two nearly orthogonal optical beams whose frequency difference Δf determines the moving lattice speed (see Appendix A). The lattice geometry is skewed to gravity and the ODT, as elaborated upon in Appendix B. Our initial BEC has a fractional population $\rho_0 \approx 0.5$ of atoms in the $|S = 1, m = 0\rangle$ state and zero magnetization (equal populations in the $|S = 1, m = \pm 1\rangle$ states). The BEC is then adiabatically loaded into the lattice, which is static for time $t < t_1$ and quenched to the desired speed at $t = t_1$ [see Fig. 1(i)]. Here, a "static" lattice is a lattice with time-independent frequency difference, i.e., $\Delta f = 0$, regardless of whether or not the lattice depth u_L is time dependent. We study the ensuing nontrivial spin (Fig. 1) and spatial (Fig. 2) dynamics of the atoms by holding them in the moving lattice until a time t_F. Similar to our previous works, we employ a two-stage microwave imaging method to obtain a spin-resolved measurement with resonant microwave pulses after releasing atoms and letting them ballistically expand for a certain time of flight (TOF) [7–9].

We first study the nonequilibrium spin dynamics generated by experimental sequences [Fig. 1(i), $\Delta f = 4.6E_R/h$], which near-resonantly couple the initial stationary $\mathbf{p} = 0$ BEC with the $\mathbf{p} = 2\hbar\mathbf{k}_L$ momentum state. Here, E_R is the recoil energy, h ($\hbar$) is the (reduced) Planck constant, and $\mathbf{k}_L$ is the lattice vector (see Appendix A) [6]. Spin-mixing oscillations, arising from coherent interconversions among two $m = 0$ atoms and a pair of atoms in the $m = \pm 1$ Zeeman states [3], constitute a useful tool in understanding the spin dynamics. The periods T of these oscillations are determined by the competition between c_2 and q, illustrated by typical examples of the interaction dominated region [Fig. 1(a)] and Zeeman dominated region [Fig. 1(c)]. We also see convincing experimental signatures of a critical separatrix regime near $q = q^*$ where T diverges [see Fig. 1(b)]. Here, q^* represents the critical quadratic Zeeman energy that separates the interaction-dominated and the Zeeman-dominated regimes. A similar phenomenon has also been observed in free space (i.e., without lattice) where the established sSMA model, which assumes $c_2(t)$ is time independent, predicts q^* to be approximately equal to c_2 for our initial state [3,11,23,24,28,31]. Our moving lattice data in Fig. 1(g) display periods that are consistent with the sSMA expectations, which can be used to estimate the effective static spin-spin interaction $c_{2,\mathrm{fit}} = h \times 23.7(1)\,\mathrm{Hz} \approx q^*$.

However, direct comparisons to the sSMA predicted time traces [dotted lines in Figs. 1(a)–1(c)] demonstrate that the model fails to capture experimentally observed features such as the damping of the oscillation amplitude and the drift of the oscillations. Another notable observation that cannot be explained by the sSMA is the shift of the separatrix location induced by the moving lattice, as shown by a comparison between static ($\Delta f = 0$) and moving lattice results in Fig. 1(a). This comparison indicates that for static lattices at an identical q in the interaction dominated regime T is smaller and thus, using the same sSMA interpretation, would lie on a curve shifted to higher q (indicating a larger characteristic c_2) relative to the moving lattice data shown in Fig. 1(g). These experimental observations suggest that the sSMA provides an incomplete description of our system.

III. THEORETICAL MODEL: DYNAMICAL SINGLE SPATIAL-MODE APPROXIMATION

To explain the sSMA's shortcomings, we develop the more versatile dSMA model, which assumes that c_2 varies with time and describes our N-particle system with the spin Hamiltonian (see Appendix D) [6,22,39]:

$$\hat{H}_{\mathrm{eff}}(t) = \frac{c_2(t)}{2N}\hat{\mathbf{S}}\cdot\hat{\mathbf{S}} + q(\hat{n}_1 + \hat{n}_{-1}). \tag{1}$$

Here, $\hat{\mathbf{S}} = \sum_{i=1}^{N}\hat{\mathbf{s}}_i$ where $\hat{\mathbf{s}}_i$ denotes the spin-1 operator for the ith atom and $\hat{n}_m$ is the number operator for the Zeeman state m. The time-dependent $c_2(t)$ arises from the temporal evolution of the BEC's spatial density profile and, in turn, modulation of the effective interaction strength of the spin model, driven by the moving lattice. Formally, $c_2(t)$ emerges from the time dependence of the Gross-Pitaevskii (GP) orbitals $\psi_m(\mathbf{r}, t)$ that describe the spatial dynamics of the mth Zeeman component.

We assume that the spatial density profile of each Zeeman component is the same but time dependent, i.e., $|\psi_m(\mathbf{r}, t)|^2 \propto |\phi(\mathbf{r}, t)|^2$, to obtain $c_2(t) \propto (N-1)\int d^3\mathbf{r}\,|\phi(\mathbf{r}, t)|^4$ (see Appendix D). This assumption is motivated by experimental observations (see Appendix E) and further justified by the qualitative agreement between theory and experiment as shown in Sec. IV. The replacement of the spatial density profiles $|\psi_m(\mathbf{r}, t)|^2$ with a common m-independent function implies that, within the dSMA, the spatial degree of freedom may contribute to the spin dynamics through $c_2(t)$ but that the spin degree of freedom does not feed back onto the evolution of the spatial profile as it is explicitly assumed to be identical for all three Zeeman components. Specifically, the common m-independent mean-field wave function $\phi(\mathbf{r}, t)$ evolves according to a spin-independent single-component GP equation that involves contributions only from the external potentials and the spin-independent density-density interactions, which are much larger than the spin-dependent interactions (see Appendix D). A key result of the presented experiment-theory work is that the dSMA enables a transparent understanding of the nontrivial spin dynamics triggered by violent spatial evolution of the BEC that occurs on faster characteristic timescales than the spin dynamics.

IV. SPATIAL DYNAMICS

To illustrate the typical spatial dynamics driving the spin mixing observed in Fig. 1, we show experimental BEC momentum distributions in Figs. 2(a)–2(c), which capture the emergence of violent spatial motion due to momentum kicks generated by the moving lattice and the shallow ODT harmonic confinement on a timescale significantly shorter than the observed spin dynamics. The rapid appearance of many discrete momentum peaks and associated spatial dynamics shown in Fig. 2 simultaneously suggests that the deviations from sSMA predictions in Figs. 1(a)–1(c) are to be expected but also entices us to reconcile elements of the good qualitative agreement between the experimental data and sSMA calculations in Fig. 1(g). We note that the creation of the discrete momentum peaks is a coherent process and does not conflict with the assumption of the single spatial-mode approximation. In fact, Fig. S1 of the Supplemental Material [48] shows that Figs. 1(a)–1(c) are very similar if different momentum components are used to construct ρ_0, thereby providing experimental support for dSMA.

To gain further insight, we use numerical GP calculations (see Appendix C), which provide a mean-field description of the full spinor BEC dynamics including both spatial and spin degrees of freedom. The complexity of the experimental system, in particular the disparate timescales of spin and spatial dynamics, precludes a full quantitative three-dimensional (3D) GP treatment. Instead, we use a reduced dimensionality 1D spinor GP calculation with parameters tuned to capture essential aspects of the experimental 3D system. This simplified treatment enables us to develop a qualitative understanding of the experimental results (see Appendix C). The GP simulations [solid lines in Figs. 1(d)–1(f)] qualitatively replicate the coherent spin dynamics, including a diverging oscillation period for $q \approx q^*$ [Fig. 1(e)] and robust harmonic oscillations for $q < q^*$ [Fig. 1(d)] and $q > q^*$ [Fig. 1(f)] with damped amplitude and drifting mean value, respectively. We note that the upward drifting mean value in the experimental data for $q > q^*$ [Fig. 1(c)], notably not captured by the 1D GP theory, may be induced by a subtle resonance mechanism between the spin and spatial dynamics [31] that depends sensitively on the dimensionality of the system. Higher dimensionality calculations will be presented elsewhere [49].

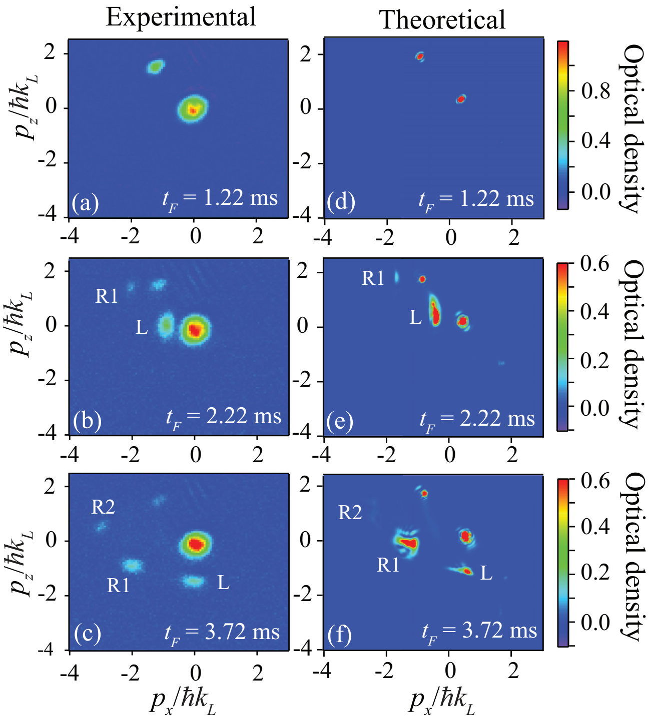

FIG. 2. Time-of-flight snapshots of 2D integrated momentum distribution with $\Delta f = 4.6E_R/h$, $u_L = 1.2E_R$, $t_1 = 0.72$ ms, and $t_F = 1.22$ ms (a), 2.22 ms (b), and 3.72 ms (c) in a shallow ODT with $L_{\mathrm{ODT},z} = 20\,\mu$m (see Appendix B) at $q/h = 42$Hz. (d)–(f) Analogous theoretical results of *in situ* momentum distributions based on 2D GP simulations (see Appendix C). The colorbar scale indicates the optical density of the images for each row.

We use GP calculations to make a more fine-grained theoretical investigation of the relationship between the spatial and spin dynamics and, in particular, certify that while the BEC undergoes violent motion on fast time-scales (i) all Zeeman components are described by a common spatial density profile $|\phi(\mathbf{r}, t)|^2$ and (ii) the combination of the moving lattice and ODT drives complex dynamics of $c_2(t)$. These observations lead us to self-consistently compare the 1D GP results to dSMA predictions, i.e., mean-field dynamics based on Eq. (1) with $c_2(t)$ computed via the GP density $|\phi(\mathbf{r},t)|^2$ (see Appendix D). The GP and dSMA time traces in Figs. 1(d)–1(f) show excellent agreement with each other.

GP calculations of the spatial dynamics in the presence of a moving lattice lead to appreciable variation of $c_2(t)$ [red line in Fig. 1(h)] at $t \lesssim 3$ ms. Over longer timescales, $c_2(t)$ features an overall decrease, which we understand as being driven by the relaxation of the spatial density profile as the BEC fractures into many momentum components. This behavior is in stark contrast with predictions for a static lattice [black line in Fig. 1(h)] that indicate $c_2(t)$ instead fluctuates around a well-defined time-averaged value with small oscillations due to excitations created during the loading phase. After the initial transient behavior in the moving lattice, our results [Fig. 1(h)] indicate that the decay of $c_2(t)$ is slow relative to the characteristic time of the spin dynamics, and therefore observables such as the spin oscillation period are captured by the sSMA (see Appendix D). Our calculations show that the precise details of the spin dynamics [e.g., qualitative features including damping of the spin oscillations in Fig. 1(a)] can depend greatly on the temporal variation of $c_2(t)$ and hence a more rigorous description is provided by the GP and dSMA models.

The precise evolution of the spatial density profile, seen in Figs. 2(a)–2(c) as a menagerie of seemingly irregularly distributed wave packets in momentum space, can be understood with the aid of GP simulations [Figs. 2(d)–2(f)]. To more precisely capture the impact of gravity and the finite trap depth, the simulations in Fig. 2 are performed using an axially symmetric two-dimensional (2D) setup. This numerical treatment is feasible due to the relatively short timescales over which the spatial dynamics are studied in detail. Two-dimensional simulations also enable us to capture key details of the momentum kicks that 1D simulations, such as those employed in Fig. 1, miss. At short times, the lattice kicks atoms from the initial BEC with momentum $\mathbf{p} = 0$ to the near-resonant state with momentum $\mathbf{p} = 2\hbar\mathbf{k}_L$ [Figs. 2(a) and 2(d)]. Subsequently, an additional momentum component, referred to as the lead peak (L peak), splits from the $\mathbf{p} = 2\hbar\mathbf{k}_L$ peak and decelerates as it travels away from the minima of the relatively shallow ODT potential. As the L peak slows, its momentum evolves until it sweeps through the approximate resonance region centered on the line $p_z \approx 0.86 p_x + 0.20\hbar k_L$ [see the gray shaded region in Fig. 3(b)], where the lattice couples two nearly resonant momentum states, corresponding to the L peak and a new peak labeled $R1$, that are separated by another $2\hbar\mathbf{k}_L$ momentum kick [Figs. 2(b) and 2(e)]. Similarly, the $R1$ peak also decelerates until it crosses the resonance region and the lattice generates a new peak labeled $R2$ [Figs. 2(c) and 2(f)]. This pattern continues and the BEC fractures into a multitude of momentum states.

Figure 3 confirms our prior analysis, which suggests a dependence on both the confining ODT potential and moving lattice, by tracking the position of the L and $R1$ peaks in time and momentum space in a compressed ODT. The position of the L peak initially follows a trajectory consistent with a Lissajous curve derived from a simplified classical treatment of a single particle initially moving with momentum $2\hbar\mathbf{k}_L$ in the ODT (see Supplemental Material [48]). A sudden momentum kick imparted by the lattice couples the L and $R1$ peaks as the former crosses the approximate resonance region, shown by the gray region in Fig. 3(a) (see Supplemental Material [48]). As time increases (i.e., deeper into the trajectory of each peak), the agreement between the experimentally observed and the theoretically predicted trajectories for the L and $R1$ peaks deteriorates, as shown near the end of the time axis in Fig. 3(b). The deterioration is most clearly seen when comparing an ideal (effectively $L_{\mathrm{ODT,i}} = \infty$) harmonic trap with our typical shallow ODT depth that features a comparatively small curvature (see Appendix E). In Fig. 3, we use a compressed ODT instead of the shallow ODT, trading reduced visibility and condensate fraction, to better illustrate the bending of the trajectory in the p_x-p_z plane (see Appendix E).

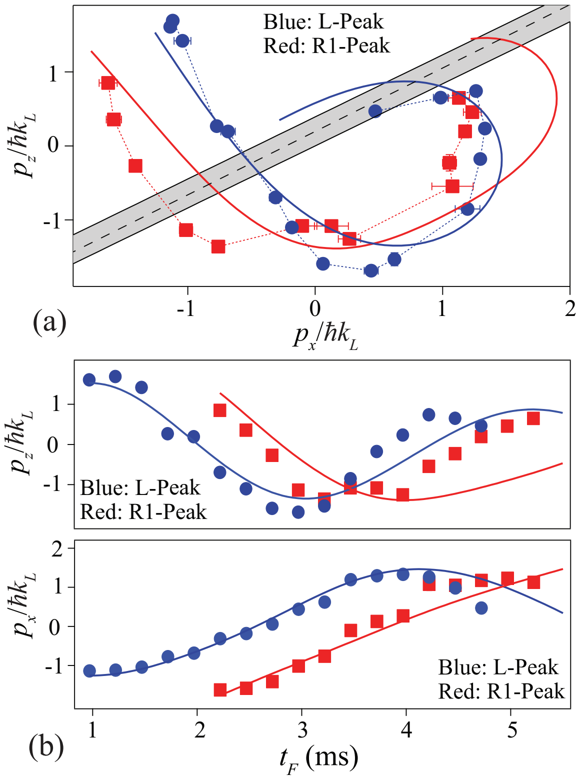

FIG. 3. (a) Trajectories of the mean position of the L peak (circles) and $R1$ peak (squares) in the $p_z - p_x$ plane taken in a compressed ODT with $L_{\mathrm{ODT},z} = 33\,\mu\mathrm{m}$ (see Appendix B), extracted from experimental images similar to those shown in Figs. 2(a)–2(c) at $q/h = 42$Hz. The gray shaded region encompasses an approximate resonance region where decelerated atoms are kicked by the lattice (to create, e.g., the $R1$ peak) (see Supplemental Material [48]). (b) The top (bottom) panel represents time evolution of p_z (p_x) momentum of the L and $R1$ peaks shown in panel (a).

V. CONCLUSION

Our results may open a new direction for the exploitation of spatial dynamics as a control knob for simulations of many-body quantum spin models with tunable, time-dependent interactions [46,47]. This is complementary to other established experimental methods, for example using microwave dressing fields to tune the quadratic Zeeman energy q as demonstrated in our prior work [11], and may be desirable for situations in which high stability of q is required. Tailored modulation of the spatial profile could be used to control the precise time dependence of the spin-spin interactions and realize Floquet-driven spin dynamics [50,51]. This can have immediate applications for the dynamical generation of entangled spin states for quantum-enhanced sensing [36,39,52–54]. The observed short-time dynamics also raise intriguing questions about equilibration of spinor BECs. For example, future studies might utilize the time dependence of $c_2(t)$ to force these systems along different equilibration trajectories.

ACKNOWLEDGMENTS

D.B. acknowledges support by NSF Grant No. PHY-2110158. R.J.L.-S. acknowledges support by NSF Grant No. PHY-2110052 and the Dodge Family College of Arts and Sciences at the University of Oklahoma (OU). Z.N.H-S., J.O.A., and Y.L. acknowledge support by the Noble Foundation and NSF Grants No. PHY-1912575 and No. PHY-2207777. This work used the OU Supercomputing Center for Education and Research.

APPENDIX A: EXPERIMENTAL SEQUENCE

Our experimental sequences start by creating a $S = 1$ spinor BEC of up to 10^5 sodium (^{23}Na) atoms in a crossed, anisotropic harmonic ODT at a particular quadratic Zeeman shift q tuned by external magnetic fields, similar to our previous work [6,9,11]. We apply a resonant rf pulse to prepare an initial state with fractional population $\rho_0 = \langle \hat{n}_0 \rangle / N \approx 0.5$ in the $|S = 1, m = 0\rangle$ state and zero magnetization, $M = \langle \hat{n}_1 - \hat{n}_{-1} \rangle / N = 0$. We then adiabatically load the initial state into a one-dimensional moving optical lattice. The lattice is constructed from two nearly orthogonal lattice beams originating from a single-mode laser with wavelength 1064 nm and characterized by the potential $V_{\text{lat}}(\mathbf{r}, t) = u_L \cos^2[\mathbf{k}_L \cdot \mathbf{r} - 2\pi \Delta f(t) t/4]$, with lattice vector $\mathbf{k}_L$ oriented at approximately 40° from the z axis defined by gravity. The resulting standing-wave potential has a lattice spacing of $\lambda_L/2 = 0.81$ μm. The time-dependent frequency difference $\Delta f(t) = |f_H - f_V|$, where f_H and f_V are the corresponding lattice beam frequencies, determines the velocity v of the moving lattice, $v = \lambda_L(f_H - f_V)$. The velocity v is manipulated via a linear ramping rate $\alpha = \frac{h[\Delta f(t_2) - \Delta f(t_1)]}{t_2 - t_1}$ such that when $v < 0$ ($v > 0$) the atoms move in the $\mathbf{p} = 2\hbar\mathbf{k}_L$ ($\mathbf{p} = -2\hbar\mathbf{k}_L$) direction. The data in Fig. 1 were taken with positive velocities, while the data in Figs. 2 and 3 were taken with negative velocities. The value of Δf is initially set to zero and, after an adiabatic ramp of the lattice depth u_L to its final value at $t = t_1$, is quenched to its final value. The total time the atoms spend in the lattice is denoted by t_F [for details see Fig. 1(i)]. At the conclusion of each sequence, the trapping potentials are turned off so that the atoms can ballistically expand and be captured using a two-step microwave imaging after a given TOF [9]. Each data point in this paper is an average of at least eight repeated measurements and all error bars reported are estimated one standard deviation.

APPENDIX B: OPTICAL DIPOLE TRAP

An essential element of our experimental setup is a harmonic confinement potential skew to the moving lattice potential. The interplay of these two potentials triggers the nontrivial spatial dynamics that are key to our findings. The harmonic confinement is provided by a crossed ODT constructed by two orthogonal beams with wavelength $\lambda = 1064$ nm. One ODT beam (ODT1) is orthogonal to gravity while the other (ODT2) is at a 76° angle relative to gravity [see Figs. 4(a) and 4(b)]. ODT1 is along the x_{ODT} axis, while the projection of ODT2 into the plane normal to gravity falls along the y_{ODT} axis [see Figs. 4(a) and 4(b)]. The moving lattice lies 72° horizontally from ODT1 and is tilted at a 40° angle relative to gravity. Due to experimental considerations, our theoretical calculations therefore occur in three distinct coordinate systems that share a common z axis defined by gravity: the coordinate systems defined by the ODT potential, the moving lattice, and the imaging plane, as illustrated in Figs. 4(a) and 4(b).

The potential generated by our crossed ODT can be parametrized to a good approximation by

$$V_{3\text{D}}(x_{\text{ODT}}, y_{\text{ODT}}, z) = -V_0 \left\{ \frac{1}{1 + \frac{x_{\text{ODT}}^2}{z_0^2}} \exp\left[\frac{-2\left(y_{\text{ODT}}^2 + z^2\right)}{\xi_0^2\left(1 + \frac{x_{\text{ODT}}^2}{z_0^2}\right)} \right] + \frac{1}{1 + \frac{y_{\text{ODT}}^2}{z_0^2}} \exp\left[\frac{-2\left(x_{\text{ODT}}^2 + z^2\right)}{\xi_0^2\left(1 + \frac{y_{\text{ODT}}^2}{z_0^2}\right)} \right] \right\}, \tag{B1}$$

where $V_0 = \frac{\mathcal{P}_0 h \alpha_{\text{FS}} \lambda^2 {\lambda_{\text{Na}}}^2}{2\pi^3 m_e c^2 \xi_0^2 (\lambda^2 - {\lambda_{\text{Na}}}^2)}$, $\xi_0 = 33$ μm is the ODT beam waist, $z_0 = \frac{\pi \xi_0^2}{\lambda}$ is the associated Rayleigh length, $\mathcal{P}_0$ is the ODT power, λ_{Na} is the D_2 line of sodium atoms, λ is the wavelength of the ODT beam, m_e is the mass of an electron, h ($\hbar$) is the (reduced) Planck constant, $\alpha_{\text{FS}} \approx \frac{1}{137}$ is the fine-structure constant, g is the gravitational acceleration, and c is the speed of light [2,3]. The ODT power, $\mathcal{P}_0$, can be varied to change the effective trap depth and size.

In Fig. 4(c) we utilize Eq. (B1) and take into account the effects of gravity to generate cross-sectional cuts for the compressed ODT trap ($\mathcal{P}_0 \approx 35$ mW), which was utilized for the experiments discussed in Figs. 3(a), 3(b) and 4(d), and the shallow ODT trap ($\mathcal{P}_0 \approx 17$ mW), which was utilized for all other experimental figures and discussions. The effective trap length $L_{\text{ODT,i}}$ is defined as the difference between the values for which $V_{3\text{D}}$ takes on a local maximum and local minimum [see Fig. 4(c)] in the i-coordinate axis. Thus, the shallow trap (red solid line) is characterized by a smaller effective trap length $L_{\text{ODT,i}}$ than the compressed trap (blue dashed line), i.e., atoms with high momentum exit the shallow trap more easily than the compressed trap. Since the trapping extends over a larger spatial region for the larger $L_{\text{ODT,i}}$, the compressed trap extends the timescales over which the complex spatial dynamics can occur. However, the extended trapping times come at the cost of an increased average atom temperature, which in turn tends to reduce the coherence and condensate fractions. This is demonstrated in Fig. 4(d), which exhibits

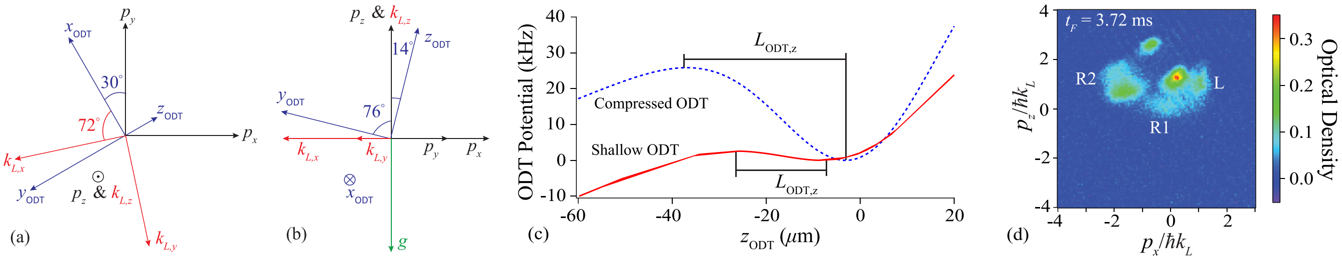

FIG. 4. (a) The three coordinate systems used in our theoretical calculations projected into the plane spanned by p_x and p_y. Blue (red) [black] axes refer to the ODT (moving lattice, with associated lattice vector $\mathbf{k}_L$) [imaging plane, with associated momentum vector $\mathbf{p}$] coordinate system. (b) Similar to (a) but projected into the plane spanned by $y_{\rm ODT}$ and $z_{\rm ODT}$. The green vector labeled by g indicates the direction of gravity. The projections in this figure are to scale. (c) Cross-sectional cut of the ODT potential after accounting for gravity in the $z_{\rm ODT}$ direction at a local minimum in the $x_{\rm ODT}$ and $y_{\rm ODT}$ directions. The effective length of the ODT along the $z_{\rm ODT}$ direction is $L_{\rm ODT,z} = 20$ μm for the shallow ODT (red solid line) and $L_{\rm ODT,z} = 33$ μm for the compressed ODT (blue dashed line). Similar plots can be made for the ODT potential in the $y_{\rm ODT}$ direction, giving an effective length of $L_{\rm ODT,y} = 31$ μm ($L_{\rm ODT,y} = 40$ μm) for the shallow (compressed) ODT. (d) Typical experimental TOF images obtained with the compressed ODT ($L_{\rm ODT,z} = 33$ μm, $L_{\rm ODT,y} = 40$ μm) displayed in panel (c). Data are taken following the same experimental sequence as in Fig. 2(c), which instead used the shallow ODT ($L_{\rm ODT,z} = 20$ μm, $L_{\rm ODT,y} = 31$ μm). The colorbar scale on the right indicates the optical density of the image.

less coherent peaks than those shown in the analogous TOF image in Fig. 2(c).

APPENDIX C: GROSS-PITAEVSKII TREATMENT OF SPIN-1 CONDENSATES

We consider a spin-1 condensate of N sodium atoms of mass $M_{\rm Na}$ under external confinement in the presence of a moving lattice. The two-body interactions are characterized by the spin-independent and spin-dependent interaction coefficients g_0 and g_2,

$$g_0 = \frac{4\pi\hbar^2(a_{S=0} + 2a_{S=2})}{3M_{\rm Na}} \tag{C1}$$

and

$$g_2 = \frac{4\pi\hbar^2(a_{S=2} - a_{S=0})}{3M_{\rm Na}}, \tag{C2}$$

where $a_{S=0} = 48.9a_0$ and $a_{S=2} = 54.5a_0$ are, respectively, the s-wave scattering lengths for the $S = 0$ and 2 states with a_0 the Bohr radius [9,55]. Our treatment includes the quadratic Zeeman shift term (proportional to q) but not the linear Zeeman shift, which does not play a role for the dynamics since it is conserved.

At the mean-field level, the coupled dynamics of the spin and spatial degrees of freedom is described by the time-dependent spinor GP equation:

$$\begin{aligned} i\hbar\frac{\partial}{\partial t}\begin{pmatrix}\psi_{-1}\\ \psi_0\\ \psi_1\end{pmatrix} &= \left[-\frac{\hbar^2\nabla^2}{2M_{\rm Na}} + V(\mathbf{r},t) + g_0(N-1)(|\psi_{-1}|^2 + |\psi_0|^2 + |\psi_1|^2)\right]\begin{pmatrix}\psi_{-1}\\ \psi_0\\ \psi_1\end{pmatrix} + \begin{pmatrix}q & 0 & 0\\ 0 & 0 & 0\\ 0 & 0 & q\end{pmatrix}\begin{pmatrix}\psi_{-1}\\ \psi_0\\ \psi_1\end{pmatrix}\\ &\quad + g_2(N-1)\begin{pmatrix}|\psi_{-1}|^2 + |\psi_0|^2 - |\psi_1|^2 & \psi_1^*\psi_0 & 0\\ \psi_1\psi_0^* & |\psi_1|^2 + |\psi_{-1}|^2 & \psi_{-1}\psi_0^*\\ 0 & \psi_{-1}^*\psi_0 & |\psi_1|^2 + |\psi_0|^2 - |\psi_{-1}|^2\end{pmatrix}\begin{pmatrix}\psi_{-1}\\ \psi_0\\ \psi_1\end{pmatrix}, \end{aligned} \tag{C3}$$

where $V(\mathbf{r},t)$ includes contributions from the moving optical lattice $V_{\rm lat}(\mathbf{r},t)$, the confining potential, and gravity. Within the GP formalism, each Zeeman component of the BEC is described by a mean-field wave function $\psi_m(\mathbf{r},t)$, such that both spin and spatial degrees of freedom, and their interplay, are simultaneously captured. The model ignores quantum fluctuations, which are expected to contribute minimally for the regimes in which the experiment operates.

For the scenarios reported, solution of the GP equation for the full 3D system by direct numerical integration is not feasible. This is due to both the disparate timescales for the spin and spatial degrees of freedom as well as the large spatial region occupied by the BEC when it is kicked by the lattice. Specifically, the repeated momentum kicks imparted by the moving optical lattice on the fractured BEC lead to intricate spatial structure as well as a rapidly expanding cloud that must be tracked over comparatively long timescales (36 ms in Fig. 1), requiring a large simulation box with good spatial resolution. Thus, the GP results presented are from numerical simulations of reduced dimensionality 1D (Fig. 1) or 2D (Fig. 2) models, wherein the interaction coefficients g_0 and g_2, mean spatial density of the BEC, and trapping potential $V(\mathbf{r},t)$ are adjusted to capture the features of the experimental setup. The GP results presented are generated by numerically integrating the coupled GP equations using the XMDS2 software package [56].

The dynamics shown in Figs. 2 and 3 are restricted to a few ms, i.e., much shorter times than those on which the spin oscillation dynamics occurs (see Fig. 1). These dynamics out to 3 ms are amenable to 2D GP equations. To this end, we define

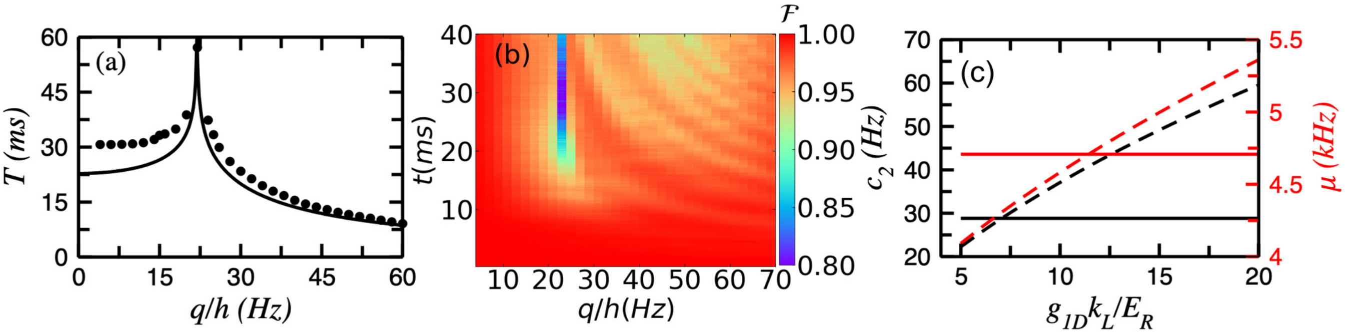

FIG. 5. (a) Spin oscillation period T as a function of Zeeman shift q. The black markers show T extracted from 1D spinor GP calculations that account for the spin-independent and spin-dependent interactions. The spin oscillation period diverges around $q^*/h = 22$ Hz. Emulating the analysis of the experimental data shown in Fig. 1(g), the solid line is obtained by fitting the 1D GP data using the analytical sSMA expressions and treating the spin-spin interaction as a fitting parameter (namely, $c_{2,\text{fit}}$). (b) Time evolution of the overlap of the Zeeman states [see Eq. (D5)] as a function of the Zeeman shift q. An overlap $\mathcal{F}$ of 1 indicates that all Zeeman states share a common spatial density profile, consistent with the dSMA. The only significant deviation from unity is observed for relatively long times ($t \gtrsim 20$ ms) when $q \approx q^*$. (c) Parameter calibration of the reduced dimensionality 1D GP equation. The black and red solid horizontal lines show the interaction energy c_2 (left axis) and chemical potential μ (right axis), respectively, for a 3D scalar BEC in the presence of a static lattice with $u_L = 2.3\ E_R$ for $N = 80\,000$ and angular trapping frequencies $\omega_x = 125$ Hz, $\omega_y = 125$ Hz, and $\omega_z = 155$ Hz. The red and black dashed lines show c_2 and μ, obtained by solving the 1D scalar GP equation as a function of the 1D coupling constant $g_{1\text{D}}^{\text{eff}}$. The 1D calculations use $\omega_z = 197$ Hz and $u_L = 2.3\ E_R$.

a "2D simulation plane" by the direction of the p_x-p_z imaging plane. The reduced dimensionality trap $V_{2\text{D}}$ is obtained by projecting the 3D trap $V_{3\text{D}}$ onto the 2D simulation plane. Our simulations capture the role of the ODT trap (including, e.g., nonharmonic corrections to the confining potential) and its interplay with gravity. Approximating the azimuthal and polar angles introduced in Appendix B by 30° and 76°, respectively, the 2D trap is given by

$$V_{2\text{D}}(y, z) = V_{3\text{D}}[\cos(76^\circ)\cos(30^\circ)y, -\sin(30^\circ)y, \sin(76^\circ)z]. \tag{C4}$$

The projection of the moving lattice in the p_x-p_y plane is described by $k_{L,x}$ [see Figs. 4(a) and 4(b)]. Neglecting the 12° angle between the $k_{L,x}$ axis and the negative p_x axis, the moving lattice is in the p_x-p_z plane. Given the fact that the lattice has a 40° angle relative to the p_z axis [see the discussion above Figs. 4(a) and 4(b)], the lattice vector is described by $\mathbf{k}_L = k_L[-\sin(40^\circ), 0, \cos(40^\circ)]$. The reduction from three dimensions to two dimensions does change the mean density and, correspondingly, the chemical potential. This is accounted for by introducing the effective 2D interaction strength $g_{2\text{D}}^{\text{eff}}$; similar to the 1D case, $g_0(N-1)$ and $g_2(N-1)$ are replaced by $g_{2\text{D}}^{\text{eff}}$ and $g_{2\text{D}}^{\text{eff}}/28.06$, respectively. The coupling constant $g_{2\text{D}}^{\text{eff}}$ is set by enforcing that the chemical potential of the 2D system, obtained by solving the scalar GP equation, is equal to that of the 3D system at $t = 0$. It should be noted that the TOF images in Figs. 2(d)–2(f) generated using this reduced 2D system are characterized by a vanishing momentum component, which does not reside exactly at $\mathbf{p} = 0$. This micromotion can be understood as a second-order effect due to the combination of the coupling between the finite and the vanishing momentum components and the force exerted on the finite-momentum component by the trap. The trap force imparts momentum to the finite-momentum BEC, which is transferred back to the zero-momentum BEC, thereby explaining the observed micromotion.

The procedure for mapping the full 3D system to a reduced dimensionality model is not unique. Figure 5(c) illustrates an example for the 1D case. Since the chemical potential μ is the characteristic energy scale of the time-independent scalar GP equation and c_2 is the characteristic energy scale of the effective spin Hamiltonian, it is natural to demand that the reduced dimensionality scalar GP model reproduces these two energy scales. The solid and dashed horizontal lines in Fig. 5(c) show the chemical potential μ and the spin-spin interaction strength c_2 of the 3D system in the presence of a static optical lattice with $u_L = 2.3\ E_R$ (note that the initial-state preparation within the full 3D framework is significantly simpler than tracking the time evolution); this is the final lattice depth used in the experiment. Fixing the parameters of the scalar 1D GP equation requires setting the values of $\hbar\omega_z/E_R$ and $g_{1\text{D}}^{\text{eff}}/(E_R k_L^{-1})$. The 1D scalar GP equation is given by Eq. (D2) with the $\mathbf{r}$ vector replaced by z and $g_0(N-1)$ replaced by $g_{1\text{D}}^{\text{eff}}$, where $g_{1\text{D}}^{\text{eff}}$ has units of "energy times length." The 1D spinor GP equation is obtained analogously, i.e., $g_0(N-1)$ and $g_2(N-1)$ are replaced by $g_{1\text{D}}^{\text{eff}}$ and $g_{1\text{D}}^{\text{eff}}/28.06$, respectively.

The black and red dashed lines in Fig. 5(c) show c_2 and μ as a function of $g_{1\text{D}}^{\text{eff}}/(E_R k_L^{-1})$ for fixed $\hbar\omega_z/E_R$ (plugging in $u_L = 2.3\ E_R$, this corresponds to $\omega_z = 197$ Hz). It can be seen that the dashed lines cross the solid lines at $g_{1\text{D}}^{\text{eff}}/(E_R k_L^{-1}) \approx 7$ and 12.5, respectively, i.e., for the $\hbar\omega_z/E_R$ value chosen there exists no unique $g_{1\text{D}}^{\text{eff}}/(E_R k_L^{-1})$ at which the values of c_2 and μ calculated within the 1D framework agree with the respective values calculated within the 3D framework. Since we do not find a unique $g_{1\text{D}}^{\text{eff}}/(E_R k_L^{-1})$ for other values of $\hbar\omega_z/E_R$ either, there exists—unless additional conditions are added—an arbitrariness in the chosen 1D simulation parameters. With this in mind, we select parameters that place the divergence of T at about the same q value as observed experimentally [see Fig. 5(a)]. Specifically, the simulations shown in Figs. 1(d)–1(f) and 5(a) use the same final lattice depth as the experiment (namely, $u_L = 2.3\,E_R$), $\omega_z = 197\,\text{Hz}$, and $g_{1\text{D}}^{\text{eff}}/(E_R k_L^{-1}) = 12.0$.

APPENDIX D: SINGLE SPATIAL-MODE APPROXIMATION AND EFFECTIVE SPIN MODEL

We now motivate and introduce an approximate treatment that decouples the spin and spatial degrees of freedom. Typically, the energy scales associated with the spin-independent terms of the Hamiltonian (i.e., the energy scales of the external harmonic and lattice confinement, the interactions that are proportional to g_0, and the chemical potential μ of the system) are of the order of kilohertz and much larger than those of the spin-dependent terms of the Hamiltonian (i.e., the value of the Zeeman shift q and the interactions that are proportional to g_2), which are of the order of hertz. This scale separation motivates an approximate treatment wherein the spin and spatial degrees of freedom are treated independently [22], with the spatial degree of freedom controlled solely by the spin-independent terms of the Hamiltonian and the spin dynamics governed by the spin-dependent terms of the Hamiltonian.

Following the literature [3], we make a single spatial-mode approximation (SMA) wherein the bosonic field operators are decomposed as

$$\hat{\psi}_m(\mathbf{r}) = \hat{a}_m \phi(\mathbf{r}, t), \tag{D1}$$

where $\hat{a}_m$ ($\hat{a}_m^\dagger$) is a bosonic operator that destroys (creates) a particle in Zeeman state m in a spatial mode defined by the spatial mean-field wave function $\phi(\mathbf{r}, t)$, which is normalized to 1, i.e., $\int d^3\mathbf{r}|\phi(\mathbf{r}, t)|^2 = 1$; in Eq. (D1), m labels the Zeeman states ($m = 0$ and ±1). The key assumption of the SMA is that $\phi(\mathbf{r}, t)$ is identical for all three Zeeman states. The mean-field wave function $\phi(\mathbf{r}, t)$ is the solution to the time-dependent scalar GP equation

$$i\hbar\frac{\partial\phi(\mathbf{r}, t)}{\partial t} \approx \left[-\frac{\hbar^2\nabla^2}{2M_{\text{Na}}} + V(\mathbf{r}, t) + g_0(N-1)|\phi(\mathbf{r}, t)|^2\right] \times \phi(\mathbf{r}, t), \tag{D2}$$

where $V(\mathbf{r}, t)$ is the same as in Eq. (C3). The spin dynamics, in turn, is governed by the effective Hamiltonian $\hat{H}_{\text{eff}}(t)$:

$$\hat{H}_{\text{eff}}(t) = \frac{c_2(t)}{2N}\hat{\mathbf{S}}\cdot\hat{\mathbf{S}} + q(\hat{a}_1^\dagger\hat{a}_1 + \hat{a}_{-1}^\dagger\hat{a}_{-1}), \tag{D3}$$

where the quantity $\hat{\mathbf{S}}$ denotes a collective spin operator. The time-dependent interaction strength $c_2(t)$,

$$c_2(t) = (N-1)g_2\int d^3\mathbf{r}|\phi(\mathbf{r}, t)|^4, \tag{D4}$$

is driven by the time dependence of the spatial mean-field wave function $\phi(\mathbf{r}, t)$, i.e., the spin dynamics is governed—through the coefficient $c_2(t)$—by the spatial dynamics. In our experiment, the spatial dynamics is, to a large degree, induced by the moving optical lattice potential. The time dependence of the interaction coefficient $c_2(t)$ is distinct from prior works (e.g., Refs. [11,24,28]), which assumed that the condensate is prepared in the ground state of a static confining potential such that subsequent spatial motion is minimal and to a good approximation $|\phi(\mathbf{r}, t)|^2 = |\phi(\mathbf{r}, 0)|^2$. For this reason, we use the distinguishing nomenclature of dynamical SMA (dSMA, time-dependent c_2) and static SMA (sSMA, time-independent c_2) for our and prior works, respectively. The latter is recovered from Eq. (D3) by assuming $c_2(t) = c_2$. To zeroth order, the dynamics of the moving lattice experiments during the first few milliseconds is dominated by spatial dynamics. At later times, however, the spin degrees of freedom become increasingly important as evidenced by the observation of spin oscillations (see Fig. 1).

The dSMA is supported by our 1D spinor GP calculations. First, Fig. 1 shows good agreement between dSMA and GP predictions for $\rho_0(t)$. Second, we can explicitly validate the assumption that each Zeeman state occupies a single common spatial mode by computing the overlap:

$$\mathcal{F} = \frac{|\int dx\psi_0^*(x)\psi_1(x)|}{\sqrt{\int dx|\psi_0(x)|^2}\sqrt{\int dx|\psi_1(x)|^2}}. \tag{D5}$$

The time evolution of this quantity over a range of Zeeman shifts is plotted in Fig. 5(b). We observe that $\mathcal{F}$ remains near unity across the interaction dominated regime ($q < q^*$) throughout the timescales we investigate (up to 40 ms in the GP calculations, which is longer than the 30 ms covered by the experiment). In the Zeeman regime, the overlap remains close to unity for $t \lesssim 20$ ms before minor deviations appear. As might be expected naively, a substantial breakdown of the single spatial-mode approximation occurs in a narrow region around the critical regime, $q \approx q^*$.

The experimental spin oscillation data in Fig. 1 are analyzed using the sSMA, i.e., the mean-field equations associated with $\hat{H}_{\text{eff}}(t)$ for a time-independent spin-spin interaction coefficient. Specifically, the spin oscillation period T is extracted by fitting the experimentally measured fractional population $\rho_0(t)$ for various q with sinusoidal functions, which provide good approximations to the spin oscillation dynamics away from the critical regime where the period diverges. All fits include at least one full period of oscillation. To determine the spin-spin interaction coefficient from the extracted periods, we perform a nonlinear least-squares fit of the T-versus-q data using the analytical solutions to the mean-field equations associated with $\hat{H}_{\text{eff}}$ [57]. The fit uses $\rho_0(0) = 0.5$ and $\theta(0) = 0$ and treats c_2 as a free parameter (we denote the fit result by $c_{2,\text{fit}}$). While $\rho_0(0)$ is measured experimentally, $\theta(0)$ is not. However, based on the experimental sequence used to prepare the initial Zeeman populations we expect that $\theta(0)$ is equal to zero. Our fitting procedure yields $c_{2,\text{fit}} = h \times 23.7(1)\,\text{Hz}$.

To gain additional insights, we perform an analogous analysis for the spin oscillation data obtained by solving the 1D spinor GP equations. Specifically, we obtain $\rho_0(t)$ and the associated period T by solving the spinor GP equations [see markers in Fig. 5(a)], and then extract $c_{2,\text{fit}}$ from the T-versus-q data using the sSMA [solid line in Fig. 5(a)]. For the 1D spinor GP simulations shown in Fig. 5(a), the spin oscillation period diverges at $q^*/h \approx 22\,\text{Hz}$, i.e., at roughly the same value of the Zeeman energy as in the experiment. The qualitative agreement between the experimental and theoretical analysis, particularly the consistency with the sSMA results, is encouraging and suggests that the 1D spinor GP simulations provide a qualitatively correct description of the moving lattice experiments.

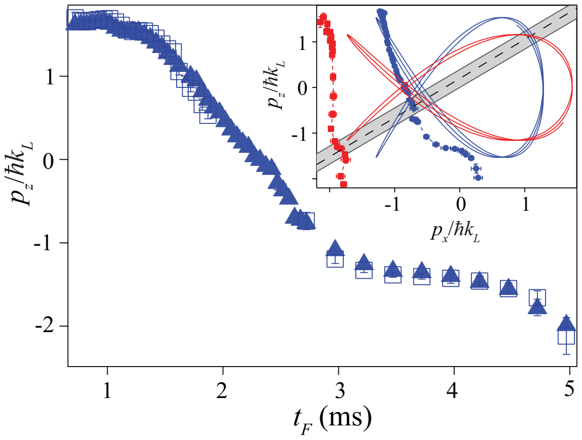

FIG. 6. Solid (open) markers represent the time evolution of the z momentum of the L peak for $m = 0$ ($m = \pm 1$) spin components extracted from experimental TOF images similar to those shown in Fig. 2. Inset: Trajectories of the mean position of L peak (blue triangles) and $R1$ peak (red squares), extracted similarly to Fig. 3. Markers represent data taken in a typical ODT ($L_{\mathrm{ODT,z}} = 20\,\mu\mathrm{m}$). Blue (red) solid lines are L peak ($R1$ peak) positions according to Lissajous curves based on a calculation of a classical point particle in an ideal (effectively, $L_{\mathrm{ODT,i}} = \infty$) harmonic trap. Preceding L peak formation, atoms occupy the $\mathbf{p} = 0$ state at $p_z = p_x = 0$ (prepared BEC) and the $\mathbf{p} = 2\hbar\mathbf{k}_L$ state. The gray shaded region marks the approximate resonance region where decelerated atoms are kicked by the lattice (to create, e.g., the $R1$ peak).

The GP simulations also enable us to better understand why the spin oscillation period extracted from the experimental data is consistent with the predictions of the sSMA, even though the time traces show significant discrepancies. In the regime $q \leqslant q^*$, the sSMA theory predicts that the spin oscillation period should be strongly correlated with the spin-spin interaction strength [6,29,57], which the GP results [see, e.g., Fig. 1(h)] predict to decay relatively slowly, compared to the typical timescales of the spin degree of freedom, apart from initial transient dynamics for $t \lesssim 3$ ms. This suggests that the spin oscillation period obtained from the experimental data for $q \leqslant q^*$ should be interpreted as being reflective of the characteristic scale of $c_2(t)$ over the experimental sequence. On the other hand, in the regime $q \gg q^*$ the oscillation period is expected to be dominated by the quadratic Zeeman shift. Thus, the experimentally observed spin oscillation periods are fit well by the sSMA predictions as the time dependence of $c_2(t)$ is less relevant for larger q.

APPENDIX E: EXPERIMENTAL COMPARISON WITH LISSAJOUS CURVES

Figure 6 shows time evolutions of spin-resolved L peak p_z momenta extracted from experimental TOF images similar to Fig. 2. The clear similarity between the $m = 0$ and ± 1 curves shown in Fig. 6 supports our previous assertion that the spatial dynamics are shared across the spin populations. As illustrated in Fig. 3, theoretical calculations of the Lissajous trajectories qualitatively reproduce the experimental trajectories that utilize the compressed ODT. However, ODT compression is accompanied by lower condensate fractions and reduced visibility [see also Fig. 4(d)]. In the inset of Fig. 6 we compare the Lissajous curves with the ODT typically employed in our experiment (uncompressed trap with $L_{\mathrm{ODT,z}} = 20\,\mu\mathrm{m}$). We find stark differences between experiment and theory curves for these parameters, including an early exiting of atoms out of the ODT trap due to gravity. The disagreements found in the compressed trap of Fig. 3 and the inset of Fig. 6 illustrate that fully capturing all the aspects of the experiment is necessarily beyond the simplified classical model, which is designed to minimally capture the dynamical appearance of resonances between different momentum states. A closer quantitative comparison would be provided by, e.g., a full 3D GP simulation and analysis of momentum space dynamics analogous to what is carried out in Fig. 3 and the inset of Fig. 6 for the experimental data.

[1] A. Polkovnikov, K. Sengupta, A. Silva, and M. Vengalattore, Colloquium: Nonequilibrium dynamics of closed interacting quantum systems, Rev. Mod. Phys. **83**, 863 (2011).

[2] I. Bloch, J. Dalibard, and W. Zwerger, Many-body physics with ultracold gases, Rev. Mod. Phys. **80**, 885 (2008).

[3] D. M. Stamper-Kurn and M. Ueda, Spinor Bose gases: Symmetries, magnetism, and quantum dynamics, Rev. Mod. Phys. **85**, 1191 (2013).

[4] M. Lewenstein, A. Sanpera, V. Ahufinger, B. Damski, A. Sen, and U. Sen, Ultracold atomic gases in optical lattices: Mimicking condensed matter physics and beyond, Adv. Phys. **56**, 243 (2007).

[5] K. Eckert, Ł. Zawitkowski, M. J. Leskinen, A. Sanpera, and M. Lewenstein, Ultracold atomic Bose and Fermi spinor gases in optical lattices, New J. Phys. **9**, 133 (2007).

[6] L. Zhao, J. Jiang, T. Tang, M. Webb, and Y. Liu, Antiferromagnetic Spinor Condensates in a Two-Dimensional Optical Lattice, Phys. Rev. Lett. **114**, 225302 (2015).

[7] J. O. Austin, Z. N. Shaw, Z. Chen, K. W. Mahmud, and Y. Liu, Manipulating atom-number distributions and detecting spatial distributions in lattice-confined spinor gases, Phys. Rev. A **104**, L041304 (2021).

[8] J. O. Austin, Z. Chen, Z. N. Shaw, K. W. Mahmud, and Y. Liu, Quantum critical dynamics in a spinor Hubbard model quantum simulator, Commun. Phys. **4**, 61 (2021).

[9] Z. Chen, T. Tang, J. Austin, Z. Shaw, L. Zhao, and Y. Liu, Quantum Quench and Nonequilibrium Dynamics in Lattice-Confined Spinor Condensates, Phys. Rev. Lett. **123**, 113002 (2019).

[10] C. Becker *et al.*, Ultracold quantum gases in triangular optical lattices, New J. Phys. **12**, 065025 (2010).

[11] L. Zhao, J. Jiang, T. Tang, M. Webb, and Y. Liu, Dynamics in spinor condensates tuned by a microwave dressing field, Phys. Rev. A **89**, 023608 (2014).

[12] K. W. Mahmud and E. Tiesinga, Dynamics of spin-1 bosons in an optical lattice: Spin mixing, quantum-phase-revival

spectroscopy, and effective three-body interactions, Phys. Rev. A **88**, 023602 (2013).

[13] L. Gabardos, B. Zhu, S. Lepoutre, A. M. Rey, B. Laburthe-Tolra, and L. Vernac, Relaxation of the Collective Magnetization of a Dense 3D Array of Interacting Dipolar $s = 3$ Atoms, Phys. Rev. Lett. **125**, 143401 (2020).

[14] S. Hild, T. Fukuhara, P. Schauss, J. Zeiher, M. Knap, E. Demler, I. Bloch, and C. Gross, Far-from-Equilibrium Spin Transport in Heisenberg Quantum Magnets, Phys. Rev. Lett. **113**, 147205 (2014).

[15] P. N. Jepsen *et al.*, Spin transport in a tunable Heisenberg model realized with ultracold atoms, Nature (London) **588**, 403 (2020).

[16] S. Smale *et al.*, Observation of a transition between dynamical phases in a quantum degenerate Fermi gas, Sci. Adv. **5**, eaax1568 (2019).

[17] J. Jiang, L. Zhao, S.-T. Wang, Z. Chen, T. Tang, L.-M. Duan, and Y. Liu, First-order superfluid-to-mott-insulator phase transitions in spinor condensates, Phys. Rev. A **93**, 063607 (2016).

[18] M. Boll *et al.*, Spin- and density-resolved microscopy of antiferromagnetic correlations in Fermi-Hubbard chains, Science **353**, 1257 (2016).

[19] L. Asteria, H. P. Zahn, M. N. Kosch, K. Sengstock, and C. Weitenberg, Quantum gas magnifier for sub-lattice-resolved imaging of 3D quantum systems, Nature (London) **599**, 571 (2021).

[20] N. A. Sinitsyn and V. Y. Chernyak, The quest for solvable multistate Landau-Zener models, J. Phys. A: Math. Theor. **50**, 255203 (2017).

[21] N. Dogra *et al.*, Dissipation-induced structural instability and chiral dynamics in a quantum gas, Science **366**, 1496 (2019).

[22] C. K. Law, H. Pu, and N. P. Bigelow, Quantum Spins Mixing in Spinor Bose-Einstein Condensates, Phys. Rev. Lett. **81**, 5257 (1998).

[23] H. Pu, C. K. Law, S. Raghavan, J. H. Eberly, and N. P. Bigelow, Spin-mixing dynamics of a spinor Bose-Einstein condensate, Phys. Rev. A **60**, 1463 (1999).

[24] S. Yi, O. E. Mustecaplioglu, C. P. Sun, and L. You, Single-mode approximation in a spinor-1 atomic condensate, Phys. Rev. A **66**, 011601 (2002).

[25] M. J. Martin *et al.*, A quantum many-body spin system in an optical lattice clock, Science **341**, 632 (2013).

[26] X. Zhang *et al.*, Spectroscopic observation of su(N)-symmetric interactions in Sr orbital magnetism, Science **345**, 1467 (2014).

[27] J. S. Krauser *et al.*, Giant spin oscillations in an ultracold Fermi sea, Science **343**, 157 (2014).

[28] Y. Liu, S. Jung, S. E. Maxwell, L. D. Turner, E. Tiesinga, and P. D. Lett, Quantum Phase Transitions and Continuous Observation of Spinor Dynamics in an Antiferromagnetic Condensate, Phys. Rev. Lett. **102**, 125301 (2009).

[29] J. Kronjager, C. Becker, P. Navez, K. Bongs, and K. Sengstock, Magnetically Tuned Spin Dynamics Resonance, Phys. Rev. Lett. **97**, 110404 (2006).

[30] H. K. Pechkis, J. P. Wrubel, A. Schwettmann, P. F. Griffin, R. Barnett, E. Tiesinga, and P. D. Lett, Spinor Dynamics in an Antiferromagnetic Spin-1 Thermal Bose Gas, Phys. Rev. Lett. **111**, 025301 (2013).

[31] J. Jie, Q. Guan, S. Zhong, A. Schwettmann, and D. Blume, Mean-field spin-oscillation dynamics beyond the single-mode approximation for a harmonically trapped spin-1 Bose-Einstein condensate, Phys. Rev. A **102**, 023324 (2020).

[32] C. Gross *et al.*, Atomic homodyne detection of continuous-variable entangled twin-atom states, Nature (London) **480**, 219 (2011).

[33] B. Lücke *et al.*, Twin matter waves for interferometry beyond the classical limit, Science **334**, 773 (2011).

[34] C. D. Hamley, C. Gerving, T. Hoang, E. Bookjans, and M. S. Chapman, Spin-nematic squeezed vacuum in a quantum gas, Nat. Phys. **8**, 305 (2012).

[35] J. Peise *et al.*, Satisfying the Einstein-Podolsky-Rosen criterion with massive particles, Nat. Commun. **6**, 1 (2015).

[36] Y.-Q. Zou *et al.*, Beating the classical precision limit with spin-1 Dicke states of more than 10,000 atoms, Proc. Natl. Acad. Sci. USA **115**, 6381 (2018).

[37] A. Qu, B. Evrard, J. Dalibard, and F. Gerbier, Probing Spin Correlations in a Bose-Einstein Condensate Near the Single-Atom Level, Phys. Rev. Lett. **125**, 033401 (2020).

[38] F. Anders, A. Idel, P. Feldmann, D. Bondarenko, S. Loriani, K. Lange, J. Peise, M. Gersemann, B. Meyer-Hoppe, S. Abend *et al.*, Momentum Entanglement for Atom Interferometry, Phys. Rev. Lett. **127**, 140402 (2021).

[39] Q. Guan, G. W. Biedermann, A. Schwettmann, and R. J. Lewis-Swan, Tailored generation of quantum states in an entangled spinor interferometer to overcome detection noise, Phys. Rev. A **104**, 042415 (2021).

[40] P. Kunkel *et al.*, Spatially distributed multipartite entanglement enables EPR steering of atomic clouds, Science **360**, 413 (2018).

[41] K. Lange *et al.*, Entanglement between two spatially separated atomic modes, Science **360**, 416 (2018).

[42] P. Kunkel, M. Prufer, S. Lannig, R. Rosa-Medina, A. Bonnin, M. Garttner, H. Strobel, and M. K. Oberthaler, Simultaneous Readout of Noncommuting Collective Spin Observables beyond the Standard Quantum Limit, Phys. Rev. Lett. **123**, 063603 (2019).

[43] P. Kunkel, M. Prufer, S. Lannig, R. Strohmaier, M. Garttner, H. Strobel, and M. K. Oberthaler, Detecting Entanglement Structure in Continuous Many-Body Quantum Systems, Phys. Rev. Lett. **128**, 020402 (2022).

[44] F. Deuretzbacher, D. Becker, J. Bjerlin, S. M. Reimann, and L. Santos, Quantum magnetism without lattices in strongly interacting one-dimensional spinor gases, Phys. Rev. A **90**, 013611 (2014).

[45] A. G. Volosniev, D. Petrosyan, M. Valiente, D. V. Fedorov, A. S. Jensen, and N. T. Zinner, Engineering the dynamics of effective spin-chain models for strongly interacting atomic gases, Phys. Rev. A **91**, 023620 (2015).

[46] E. J. Davis, G. Bentsen, L. Homeier, T. Li, and M. H. Schleier-Smith, Photon-Mediated Spin-Exchange Dynamics of Spin-1 Atoms, Phys. Rev. Lett. **122**, 010405 (2019).

[47] A. Periwal *et al.*, Programmable interactions and emergent geometry in an array of atom clouds, Nature (London) **600**, 630 (2021).

[48] See Supplemental Material at http://link.aps.org/supplemental/10.1103/PhysRevA.107.053311 for further details on the experimental setup, theory formulation and simulation, and supporting experimental and theoretical results.

[49] Q. Guan *et al.* (unpublished).

[50] K. Fujimoto and S. Uchino, Floquet spinor Bose gases, Phys. Rev. Res. **1**, 033132 (2019).

[51] Z.-C. Li, Q.-H. Jiang, Z. Lan, W. Zhang, and L. Zhou, Nonlinear Floquet dynamics of spinor condensates in an optical cavity: Cavity-amplified parametric resonance, Phys. Rev. A **100**, 033617 (2019).

[52] P. Feldmann, M. Gessner, M. Gabbrielli, C. Klempt, L. Santos, L. Pezze, and A. Smerzi, Interferometric sensitivity and entanglement by scanning through quantum phase transitions in spinor Bose-Einstein condensates, Phys. Rev. A **97**, 032339 (2018).

[53] S. S. Mirkhalaf, E. Witkowska, and L. Lepori, Supersensitive quantum sensor based on criticality in an antiferromagnetic spinor condensate, Phys. Rev. A **101**, 043609 (2020).

[54] B. Sundar *et al.*, Bosonic Pair Production and Squeezing for Optical Phase Measurements in Long-Lived Dipoles Coupled to a Cavity, Phys. Rev. Lett. **130**, 113202 (2023).

[55] S. Knoop, T. Schuster, R. Scelle, A. Trautmann, J. Appmeier, M. K. Oberthaler, E. Tiesinga, and E. Tiemann, Feshbach spectroscopy and analysis of the interaction potentials of ultracold sodium, Phys. Rev. A **83**, 042704 (2011).

[56] G. R. Dennis, J. J. Hope, and M. T. Johnsson, XMDS2: Fast, scalable simulation of coupled stochastic partial differential equations, Comput. Phys. Commun. **184**, 201 (2013).

[57] W. Zhang, D. L. Zhou, M.-S. Chang, M. S. Chapman, and L. You, Coherent spin mixing dynamics in a spin-1 atomic condensate, Phys. Rev. A **72**, 013602 (2005).